

# Prediction of texture evolution under varying deformation states through crystal plasticity finite element method

LI Hong-wei, YANG He

State Key Laboratory of Solidification Processing, Northwestern Polytechnical University, Xi'an 710072, China

Received 28 August 2012; accepted 25 October 2012

**Abstract:** An explicit model controlled by a linear equations set was developed. This model was directly solved by the complete pivot GAUSSIAN elimination method without any iteration. In addition, crystallographic-system based solving procedure was proposed to reduce the additional calculation caused by grain rotation. By establishing crystal plasticity finite element model (CPFEM), the model was verified by comparing the predicted texture to the experimental results. Then, the model was applied to predict textures under different deformation states achieved by adjusting the ratio ( $k$ ) of the loading velocities in  $Z$  and  $Y$  directions. The results show that the model is reliable in texture prediction (good agreement with the experiments in compression, tension, simple shear and plane-strain compression) and much more efficient (more than 100 times) than the implicit model; with the increasing of  $k$ , the strong texture progresses from  $\pm 35^\circ$  to normal direction to fiber texture in the  $\{111\}$  plane and enhances in intensity; the texture intensity drops dramatically when the strain rate increases from  $0.1 \text{ s}^{-1}$  to  $100 \text{ s}^{-1}$ , while drops slowly when the strain rate increases from  $100 \text{ s}^{-1}$  to  $7 \times 10^4 \text{ s}^{-1}$ , which indicates the computational stability of the model for simulation of ultra-high strain rate deformation.

**Key words:** crystal plasticity; texture evolution; deformation state; strain rate; explicit model

## 1 Introduction

Texture evolution takes place during plastic deformation of metals, which in turn results in anisotropic mechanical properties of the deformed part [1]. Additionally, texture evolution varies with different deformation states sensitively. So, texture prediction is an effective way for deformation design and performance control. Crystal plasticity model is widely known and utilized for texture prediction in metal deformation process. However, the major drawback of crystal plasticity models lies in computational issue [2], i.e. inefficient and unstable solution. The widely used Newton–Raphson (N–R) iteration approach [3–5] is computationally stable and accurate but inefficient due to massive iterations existing both at the local level to update the stress and globally to enforce equilibrium [6]. As to the implicit algorithms, rate–tangent method [7] and Euler forward method [8] are typical representatives of explicit algorithms, which promote the computational efficiency remarkably [6]. However, they were very rigid

needing very small step length [8].

On the other hand, grains aggregate should be taken into account for prediction of texture evolution. Grains interaction during deformation process is a challenging issue in crystal plasticity modeling. To the problem of no grain interaction considered in the Taylor model [9], van HOUTTE et al [10] proposed a bicrystal model, so called LAMEL model, which calculated two crystals at the same time so that to consider grain interactions. The model was improved by van HOUTTE et al [11] from LAMEL model to ALAMEL model by considering two neighboring domains, the subdivision of a grain. Subsequently, MAHESH [12] proposed a binary-tree based model to maintain traction continuity across grain interface within an aggregate by dividing the aggregate to subaggregates and then subdividing until the smallest sub-divisions contain only single grains. Similarly, KUMAR et al [13] proposed a “stack” model based on the ALAMEL model to account for intra interactions by means of an arbitrary number  $N$  of co-deforming domains. In addition, self-consistent models [14–16] consider grain interaction by allowing constraints on

**Foundation item:** Project (2011CB012802) supported by the National Basic Research Program of China; Project (51175428) supported by the National Natural Science Foundation of China; Project (B08040) supported by the Programme of Introducing Talents of Discipline to Universities (“111” Project)

**Corresponding author:** LI Hong-wei, Tel: +86-29-88460212; E-mail: [lihongwei@nwpu.edu.cn](mailto:lihongwei@nwpu.edu.cn)  
DOI: 10.1016/S1003-6326(12)61712-9

shearing directions of a grain but not applying full constraints. Also, crystal plasticity finite element model (CPFEM) [17] considers grain interactions by the nature that the nodes in finite element model are constrained by each other.

In this work, Taylor series expansion was applied to recast the high-order nonlinear equation accounting for rate dependent shear strain rate into a linear equations set. Then, an incremental explicit model was deduced with the linear equations set as the control equation. This model was solved directly by the complete pivot Gaussian elimination method, which avoids iterations in the implicit model and overcomes the shortcomings caused by the approximation adopted in aforementioned explicit models. By developing user subroutine VUMAT, this model was embedded in the commercial software ABAQUS/Explicit. The model was verified on texture prediction in axial compression, tension, simple shear and plane-strain compression through a CPFEM. Then, the model was applied to investigate texture evolution under varying deformation states and strain rates.

## 2 Crystal plasticity finite element modeling

### 2.1 Constitutive relation

The elastic constitutive relation for the stress in each grain is taken as

$$\mathbf{T}^* = \mathbf{R} : \mathbf{E}^* \quad (1)$$

where  $\mathbf{E}^* \equiv (1/2)((\mathbf{F}^*)^T \mathbf{F}^* - \mathbf{I})$  is an elastic strain measure,  $\mathbf{R}$  is a fourth-order elasticity tensor,  $\mathbf{I}$  is the second-order identity tensor.  $\mathbf{T}^*$  has the relation with  $\mathbf{T}$  as:

$$\mathbf{T}^* \equiv (\mathbf{F}^*)^{-1} \{(\det \mathbf{F}^*) \mathbf{T}\} (\mathbf{F}^*)^{-T} \quad (2)$$

where  $\mathbf{F}^* = \mathbf{F} \mathbf{F}^{p-1}$  is the non-plastic deformation gradient with the plastic deformation gradient  $\mathbf{F}^p$  evolving as  $\dot{\mathbf{F}}^p = \mathbf{L}^p \mathbf{F}^p$ .

The plastic part of velocity gradient can be calculated through the crystal plasticity theory as

$$\mathbf{L}^p = \sum_{\alpha} \dot{\gamma}^{\alpha} \mathbf{S}_0^{\alpha}, \quad \mathbf{S}_0^{\alpha} \equiv \mathbf{m}_0^{\alpha} \otimes \mathbf{n}_0^{\alpha} \quad (3)$$

where  $\mathbf{m}_0^{\alpha}$  and  $\mathbf{n}_0^{\alpha}$  are time-independent orthonormal unit vectors which define the slip direction and slip plane normal of the  $\alpha$ -th slip system in a fixed reference configuration, and  $\mathbf{S}_0^{\alpha}$  is the Schmid tensor.

### 2.2 Flow rule

The rate-dependent flow rule is adopted. The plastic shearing rate on the  $\alpha$ -th slip system can be given by an exponential type law in terms of the resolved shear stress

(RSS)  $\tau^{\alpha}$  and deformation resistance of the  $\alpha$ -th slip system  $s^{\alpha}$  as

$$\dot{\gamma}^{\alpha} = \dot{\gamma}_0 \left| \frac{\tau^{\alpha}}{s^{\alpha}} \right|^{1/m} \text{sign}(\tau^{\alpha}) \quad (4)$$

where  $\dot{\gamma}_0$  is a reference value,  $m$  is the strain rate sensitive coefficient of material, and the symbol sign stands for getting the sign symbol of  $\tau^{\alpha}$ .

In Eq. (4), RSS may be approximated by

$$\tau^{\alpha} = \mathbf{T}^* : \mathbf{S}_0^{\alpha} \quad (5)$$

### 2.3 Work hardening

The KOCKS-type hardening rule is adopted.  $s^{\alpha}$  evolves as

$$\dot{s}^{\alpha} = \sum_{\beta} h^{\alpha\beta} |\dot{\gamma}^{\beta}| \quad (6)$$

where  $h^{\alpha\beta}$  is the rate of strain hardening on slip system  $\alpha$  due to shearing on the slip system  $\beta$ , which is related to a single slip hardening rate,  $h^{(\beta)}$ , and the hardening matrix,  $\mathbf{q}^{\alpha\beta}$ , as  $h^{\alpha\beta} = \mathbf{q}^{\alpha\beta} h^{(\beta)}$  (no sum on  $\beta$  here) with  $h^{(\beta)} = h_0 [1 - s^{\beta} / s_s]^a$ . Parameters  $h_0$ ,  $s_s$  and  $a$  are hardening parameters. The hardening matrix,  $\mathbf{q}^{\alpha\beta}$ , given by ZHOU et al [18] is adopted to account for the latent hardening and self-hardening of a crystal.

### 2.4 Numerical algorithm

As described above, rate dependent crystal plasticity model contains implicit equations with respect to  $\mathbf{T}^*$  and  $\dot{\gamma}^{\alpha}$ . Moreover, Eq. (5) indicates high-level nonlinearity of this model since  $m$  is usually very small for metals (0.01–0.05). These characters bring trouble for numerical solution in computational efficiency and stability. Therefore, many research works have been done on numerical algorithms as discussed in Section 1. Here, we focus on the work presented by KALIDINDI et al [3]. In Ref. [3], a fully implicit time-integration procedure was presented and relative equations were deduced. Also, a two-level N–R iterative method was adopted for numerical solution. It was found that it was hard to find a suitable initial value for convergence of the N–R iteration in each time step in finite element calculation even though a very small step length was adopted [4]. So, we introduced a homotopy auto-changing continuation method to iterate a suitable initial value before the N–R iteration algorithm was invoked. Although this method achieved the computational stability, it is low efficient due to much iteration additionally introduced by the homotopy continuation method besides the N–R method. As a result, it was applied only in calculations with a single crystal.

Here, a novel explicit model was established based on Ref. [3]. During the modeling,  $t$  and  $\tau = t + \Delta t$  denote

the time at the start and the end of each increment, respectively. Taylor series expansion of Eq. (5), neglecting the high-order terms, is expressed as

$$\dot{\gamma}^\alpha(\tau) \approx \dot{\gamma}^\alpha(t) \left[ 1 + \frac{\delta_1}{m} \left( \frac{\Delta\tau^\alpha}{\tau^\alpha(t)} - \frac{\Delta s^\alpha}{s^\alpha(t)} \right) \right] \quad (7)$$

$$\text{with } \begin{cases} \delta_1 = 1, & \text{if } \tau^\alpha(t) \geq 0 \\ \delta_1 = -1, & \text{else} \end{cases}$$

When  $\Delta\gamma^\alpha = \dot{\gamma}^\alpha(t)\Delta t$  is assumed,  $\Delta\tau^\alpha \doteq \Delta\mathbf{T}^* : \mathbf{S}_0^\alpha$  can be simplified since  $\mathbf{S}_0^\alpha$  is unchangeable with deformation when calculations are carried out in the crystallographic system, which will be discussed in Section 2.6.

So, the increments of stress and resistance of slip systems can be deduced based on the algorithm proposed by KALINDINDI et al [3]. They take the forms as

$$\Delta\mathbf{T}^* = (\mathbf{T}^*)^{\text{tr}} - \mathbf{T}^*(t) - \sum_{\alpha} \Delta\gamma^\alpha \left[ 1 + \frac{\delta_1}{m} \left( \frac{\Delta\mathbf{T}^* : \mathbf{S}_0^\alpha}{\tau^\alpha(t)} - \frac{\Delta s^\alpha}{s^\alpha(t)} \right) \right] \mathbf{C}^\alpha \quad (8)$$

$$\Delta s^\alpha = \sum_{\beta} h^{\alpha\beta} \times \Delta\gamma^\beta \left[ 1 + \frac{\delta_1}{m} \left( \frac{\Delta\mathbf{T}^* : \mathbf{S}_0^\beta}{\tau^\beta(t)} - \frac{\Delta s^\beta}{s^\beta(t)} \right) \right] \quad (9)$$

where

$$\begin{cases} (\mathbf{T}^*)^{\text{tr}} = \mathbf{R} : \left[ \frac{1}{2} (\mathbf{A} - \mathbf{I}) \right] \\ \mathbf{C}^\alpha = \mathbf{R} : \left( \frac{1}{2} \mathbf{B}^\alpha \right) \\ \mathbf{B}^\alpha = \mathbf{A} \mathbf{S}_0^\alpha + (\mathbf{S}_0^\alpha)^{\text{T}} \mathbf{A} \\ \mathbf{A} = \mathbf{F}^{\text{p-T}}(t) \mathbf{F}^{\text{T}}(\tau) \mathbf{F}(\tau) \mathbf{F}^{\text{p-1}}(t) \end{cases} \quad (10)$$

Since all variables at time  $t$  are known, Eqs. (8) and (9) are the equations set with the unknowns of  $\Delta\mathbf{T}^*$  and  $\Delta s^\alpha$ . For the purpose of efficiency, a two-level procedure is adopted here. Firstly,  $\Delta s^\alpha$  is fixed at its value at time  $t$ , Eq. (8) can be deduced and written in its components as

$$(\delta_2 + K_{ijkl}) \Delta T_{ij}^* = H_{kl} \quad \text{with } \begin{cases} \delta_2 = 1, & \text{if } i = k, j = l \\ \delta_2 = 0, & \text{else} \end{cases} \quad (11)$$

where

$$K_{ijkl} = \sum_{\alpha} \frac{\delta_1 \Delta\gamma^\alpha (S_0^\alpha)_{ij}}{m \tau^\alpha(t)} C_{kl}^\alpha, \quad i, j, k, l \in (1, 3)$$

$$H_{kl} = (\mathbf{T}^*)^{\text{tr}}_{kl} - \mathbf{T}^*_{kl}(t) - \sum_{\alpha} \Delta\gamma^\alpha \left[ 1 - \frac{\delta_1 \Delta s^\alpha}{m s^\alpha(t)} \right] C_{kl}^\alpha$$

Since both  $K_{ijkl}$  and  $H_{kl}$  can be calculated directly, Eq. (11) is a linear equations set with the unknowns of  $\Delta T_{ij}^*$ . Here, the complete pivot Gaussian

elimination method is adopted for the solution. After getting  $\Delta T_{ij}^*$ , the second-level solving procedure starts. Equation (9) can also be rewritten into a linear equations set in the same way, expressed as

$$(\delta_3 + X_{\alpha\beta}) \Delta s^\alpha = Y_{\alpha\beta} \quad \text{with } \begin{cases} \delta_3 = 1, & \text{if } \alpha = \beta \\ \delta_3 = 0, & \text{else} \end{cases} \quad (12)$$

where

$$X_{\alpha\beta} = \frac{\delta_1 h^{\alpha\beta} \Delta\gamma^\beta}{m s^\beta(t)}$$

$$Y_{\alpha\beta} = \sum_{\beta} h^{\alpha\beta} \Delta\gamma^\beta \left( 1 + \frac{\delta_1 \Delta T_{ij}^* S_0^\beta}{m \tau^\beta(t)} \right)$$

So,  $\Delta s^\alpha$  can also be updated with the new  $\Delta T_{ij}^*$  by the complete pivot GAUSSIAN elimination method. Then, a recalculation loop is invoked for a new  $\Delta T_{ij}^*$  by the new  $\Delta s^\alpha$  until the following equations are satisfied.

$$|\Delta T_{ij}^{*(n+1)} - \Delta T_{ij}^{*(n)}| < 10^{-4} s_0 \quad (13)$$

$$|\Delta s_{(n+1)}^\alpha - \Delta s_{(n)}^\alpha| < 10^{-3} s_0 \quad (14)$$

Here,  $s_0$  is the initial deformation resistance of slip systems, and all slip systems are assumed to have the same value.

## 2.5 Texture tracking

Texture evolution is tracked through a rotation matrix  $\mathbf{Q}$ , which is formed through three Euler angles in Kalidindi's notation (see Ref. [3]). This matrix was defined to quantify the relation of vectors or tensors between the crystallographic system ( $C_c$ ) and the global system ( $C_g$ ). Taking advantage of this rotation matrix, there exist:

$$\mathbf{D}_g = \mathbf{Q} \mathbf{D}_c \mathbf{Q}^{\text{T}} \quad (15)$$

$$\mathbf{D}_c = \mathbf{Q}^{-1} \mathbf{D}_g \mathbf{Q}^{-\text{T}} \quad (16)$$

where  $\mathbf{D}_g$  stands for a tensor in  $C_g$  and  $\mathbf{D}_c$  stands for the one in  $C_c$ .

In order to track texture evolution, the matrix  $\mathbf{Q}$  should be stored and updated step by step during forming process. The equation proposed by KALINDINDI et al [3] is employed as

$$\mathbf{Q}(\tau) = \mathbf{F}^*(\tau) \cdot \mathbf{Q}(t) \quad (17)$$

where  $\mathbf{F}^*(\tau)$  is the non-plastic part of the deformation gradient at time  $\tau$ .

## 2.6 Stress update systems

Since vectors and tensors related to crystals are stored in  $C_c$ , such as  $\mathbf{S}_0^\alpha$  and  $\mathbf{R}$ , while the ones related

to deformation, such as  $\mathbf{F}$ ,  $\mathbf{E}$ ,  $\mathbf{T}$  and  $\mathbf{Q}$ , provided by the finite element method are stored in  $C_g$ . As we all know, all tensors and vectors must be in the same system during constitutive update. Therefore, the transformation between systems for vectors and tensors is needed. There are two ways for the transformation. One is to transfer the ones in  $C_c$  to  $C_g$  so as to perform constitutive update in  $C_g$ , and the other is to transfer the ones in  $C_g$  to  $C_c$  so as to perform constitutive update in  $C_c$ . However, the first way is expensive since the sizes of internal variables related to crystals increase with the increase of the number of elements ( $n_e$ ) and crystals ( $n_c$ ) at the level of  $n_e \times n_c$ . Nevertheless, the variables need to be transferred in the second way are only related to elements. Thus, all variables in  $C_g$  are transferred to  $C_c$  in this work in order for computational efficiency. In this case, tensors related to crystals are time-independent constants for all crystals so that there is much less calculation to do. Here, we have to mention that the obtained stress  $\mathbf{T}$  and orientation update matrix  $\mathbf{F}^*$  are also in  $C_c$ . Therefore, it is required to transfer them to  $C_g$  to return to finite element method and to calculate texture update.

## 2.7 Numerical procedure

According to the presented model, a user subroutine VUMAT was developed under the environment of ABAQUS/Explicit [19]. The procedure for coding is listed below.

- 1) Get known variables of  $\mathbf{F}(t)$  and  $\mathbf{F}(\tau)$  in  $C_g$ ;
- 2) Grain number ( $k$ ) starts from 1;
- 3) Get variables of  $\mathbf{Q}^\alpha$ ,  $\mathbf{F}^p(t)$ ,  $\Delta\gamma^\alpha(t)$ ,  $s^\alpha(t)$  and  $\tau^\alpha(t)$  ( $\alpha$  starts from 1);
- 4) Transfer  $\mathbf{F}(t)$  and  $\mathbf{F}(\tau)$  to  $C_c$ ;
- 5) Calculate  $\mathbf{A}$ ,  $\mathbf{B}^\alpha$ ,  $\mathbf{C}^\alpha$  and  $(\mathbf{T}^*)^{\text{tr}}$ ;
- 6) Calculate  $K_{ijkl}$  and  $H_{kl}$  with  $\Delta s^\alpha = 0$ ;
- 7) Solve Eq. (11) to get  $\Delta T_{ij}^*$ ;
- 8) Calculate  $X_{\alpha\beta}$  and  $Y_{\alpha\beta}$  with the newly obtained  $\Delta T_{ij}^*$ ;
- 9) Solve Eq. (12) to get a new  $\Delta s^\alpha$ ;
- 10) If Eqs. (13) and (14) are satisfied, go on; if not, return to Step 6 with the new  $\Delta s^\alpha$ ;
- 11) Transfer  $\Delta \mathbf{T}^*$  and  $\mathbf{F}^*$  to  $C_g$ ;
- 12) Update  $\mathbf{F}^p(\tau)$  via Eq. (3),  $\mathbf{T}^*(\tau) = \mathbf{T}^*(t) + \Delta \mathbf{T}^*$ ,  $s^\alpha(\tau) = s^\alpha(t) + \Delta s^\alpha$ ,  $\Delta\gamma^\alpha(\tau)$ ,  $s^\alpha(\tau)$  and  $\tau^\alpha(\tau)$ ;
- 13) Update  $\mathbf{Q}^\alpha(\tau)$  by Eq. (16);
- 14) If  $k > N$  (total grains), go on, otherwise,  $k = k + 1$ , return to Step 3;
- 15) Calculate the volume-average Cauchy stress on the material point  $\bar{\mathbf{T}}$ ;
- 16) Carry out the calculations of  $\mathbf{R}(\tau) \cdot \bar{\mathbf{T}} \cdot \mathbf{R}^T(\tau)$  (with  $\mathbf{R}(\tau) = \mathbf{F}(\tau) \cdot \mathbf{U}^{-1}(\tau)$ ) to meet the requirements on stress and strain in ABAQUS/Explicit;
- 17) Subroutine ends and returns.

## 2.8 Finite element modeling

A finite element model is created as shown in Fig. 1. There are 1000 C3D8R (an eight-node linear brick reduced integration and hourglass control element in ABAQUS/Explicit) elements within a 1 mm × 1 mm × 1 mm cube. The primary load is along the  $V_2$  direction and the second one is along the  $V_3$  direction. The bottom face of the cube is fixed in the  $Y$ -direction. The left and right lateral sides are with constraints which keep the surface in a plane during deformation. Thus, the effects of other neighboring materials can be simulated.

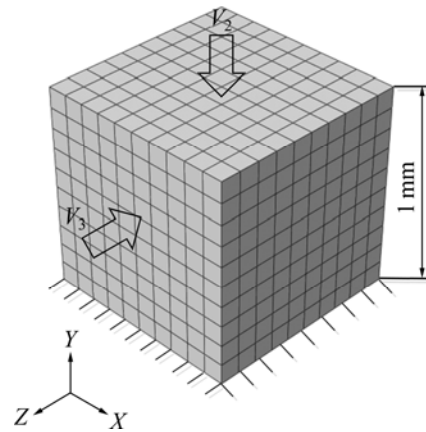


Fig. 1 Finite element meshes and loading configuration

About 1000 orientations representing the initial texture are mapped on the 1000 elements one by one. Therefore, one element stands for an individual grain and grain interactions can be taken into account from the equilibrium between neighboring elements.

## 3 Model verification

### 3.1 Initial conditions

The initial texture represented by 1000 random distributed orientations is shown in Fig. 2. Four typical forming processes are introduced to verify the model in texture prediction. They are uniaxial compression, uniaxial tension, simple shear and plane-strain compression which has the essence as sheet rolling process. The deformation in all of the processes reaches a true strain of 1.4 with the strain rate of  $1 \text{ s}^{-1}$ . The material used in simulation is oxygen free high conductivity (OFHC) copper, whose parameters are listed in Table 1. 12  $\langle 111 \rangle$ (110) slip systems are considered in the simulations.

### 3.2 Model efficiency

Uniaxial compression is calculated to study the efficiency of the model. In the simulation, the machine is a workstation with the configurations of 8 Intel Xeon CPUs @ 2.53 GHz, and 12.0 GB memory. CPU time by

using the presented algorithm (only 1 CPU used in this case) was compared with that by using the implicit algorithm proposed in Ref. [4], as listed in Table 2. In this table,  $N_e$  is element number,  $N_c$  is crystal number within one element,  $t\text{-ex}$  is the CPU time costed by the explicit model,  $t\text{-im}$  is the one costed by the implicit model, and  $\Delta t_{\max}$  and  $\Delta t_{\min}$  are the maximal and minimal time increments, respectively. The presented algorithm shows much more efficient than the implicit algorithm (more than 100 times).

### 3.3 Texture evolution in uniaxial compression

Uniaxial compression is achieved by releasing the constraint of  $V_3$  in Fig. 1. The pole figures of  $\{100\}$ ,  $\{110\}$  and  $\{111\}$  at a true strain of 1.4 are presented in Figs. 3(a), (b) and (c), respectively. The experiments carried out by BRONKHORST et al [20] are taken for comparison. Figure 3 shows that both the predictions and

**Table 1** Material constants of OFHC copper

Parameter	Value
Density, $\rho/(\text{kg}\cdot\text{mm}^{-3})$	$8.9\times 10^{-9}$
Elasticity constants, $C_{11}, C_{12}, C_{44}/\text{GPa}$	170, 124, 75
Reference value of slip rate, $\dot{\gamma}_0/\text{s}^{-1}$	0.001
Rate sensitivity coefficient, $m$	0.012
Initial critical RSS, $s_0^\alpha/\text{MPa}$	16.0
Saturation strength, $s_s/\text{MPa}$	148
Initial hardening rate, $h_0/\text{MPa}$	180
Index $a$	2.25

**Table 2** Comparable analysis of computational efficiency

$N_e$	$N_c$	$t\text{-ex}/\text{s}$	$t\text{-im}/\text{s}$	$\Delta t_{\max}/\text{s}$	$\Delta t_{\min}/\text{s}$
1000	1	15123.3	17821360.1	$1.7\times 10^{-8}$	$3.5\times 10^{-9}$

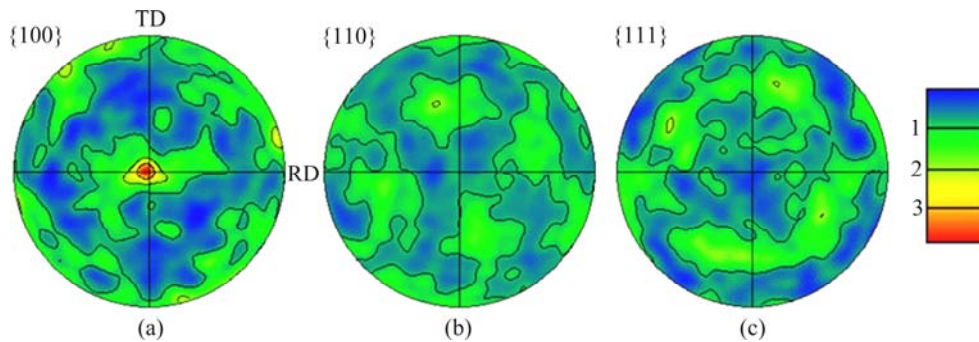


**Fig. 2** Initial texture represented by 1000 randomly distributed orientation: (a)  $\{100\}$ ; (b)  $\{110\}$ ; (c)  $\{111\}$

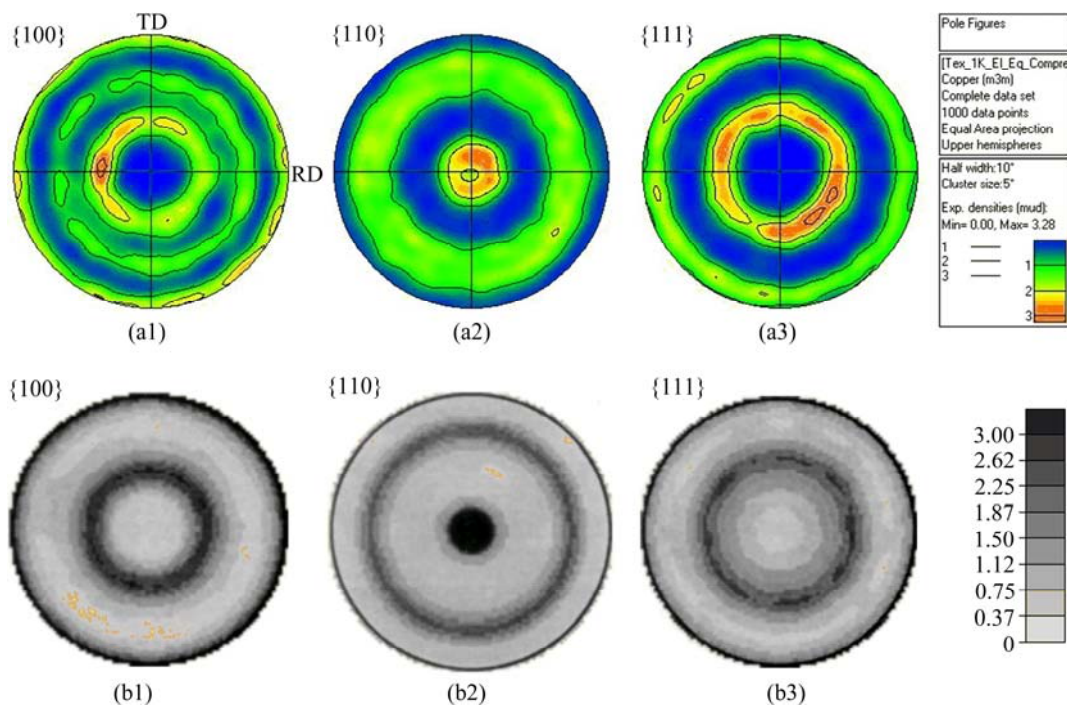


**Fig. 3** Textures in axial compression at true strain of 1.4: (a1–a3) Predictions of planes  $\{100\}$ ,  $\{110\}$  and  $\{111\}$ ; (b1–b3) Experiments of planes  $\{100\}$ ,  $\{110\}$  and  $\{111\}$  [20]

experiments capture the {110} fiber texture and {111} plane texture well. Moreover, they have the quantitatively comparability.

**3.4 Texture evolution in uniaxial tension**

By releasing  $V_3$  and reversing  $V_2$  in the model in Fig. 1, uniaxial tension is calculated for texture evolution. Figure 4 shows that both the prediction and experiment results capture the {111} fiber texture well.

**3.5 Texture evolution in simple shear**

By releasing  $V_3$  and rotating  $V_2$  by  $90^\circ$  in the model

in Fig. 1, simple shear is calculated for texture evolution. Figure 5 shows that the predictions agree with the experiments well. The highest-intensity textures occur at  $30^\circ, 90^\circ, 150^\circ, 210^\circ, 270^\circ, 330^\circ \perp$ ND on the {111} plane, respectively.

**3.6 Texture evolution in plane-strain compression**

Setting  $V_3=0$ , i.e. keeping the XY-plane fixed, the plane-strain compression is achieved. The typical textures in plane-strain compression are predicted, as shown in Fig. 6, which agree with the experiments. The highest intensity texture appears at  $\pm 35^\circ$  to ND along RD

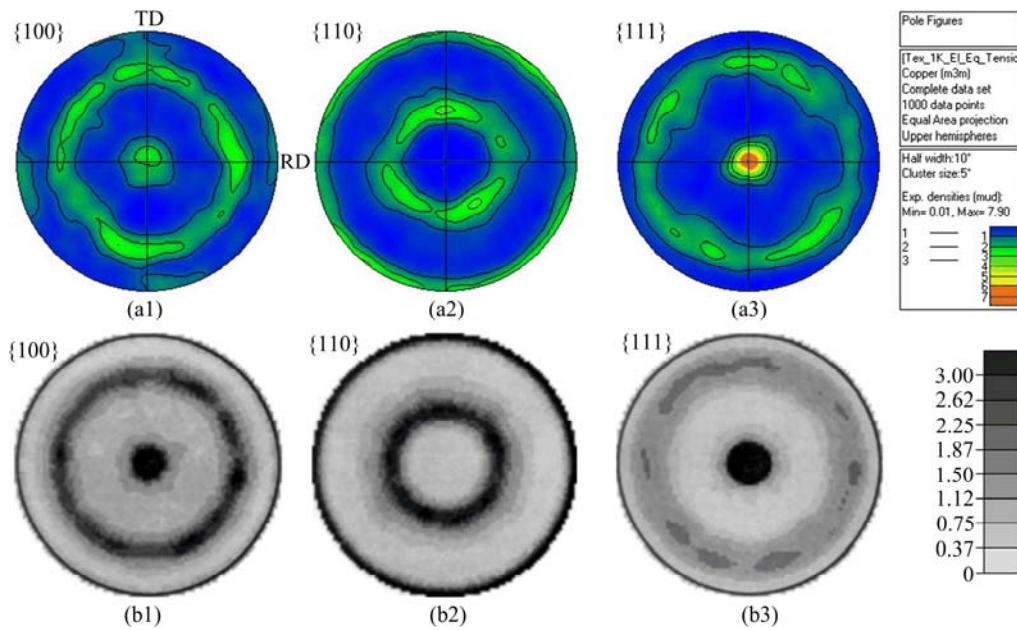


**Fig. 4** Textures in axial tension at true strain of 1.4: (a1–a3) Predictions of planes {100}, {110} and {111}; (b1–b3) Experiments of planes {100}, {110} and {111} [20]

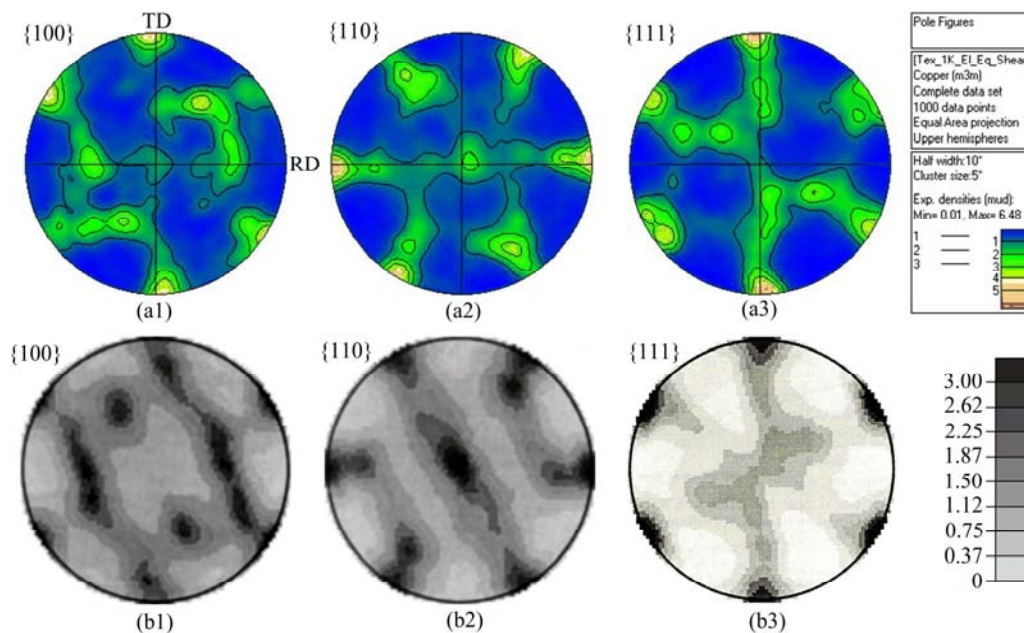


**Fig. 5** Textures in simple shear at true strain of 1.4: (a1–a3) Predictions of planes {100}, {110} and {111}; (b1–b3) Experiments of planes {100}, {110} and {111} [20]

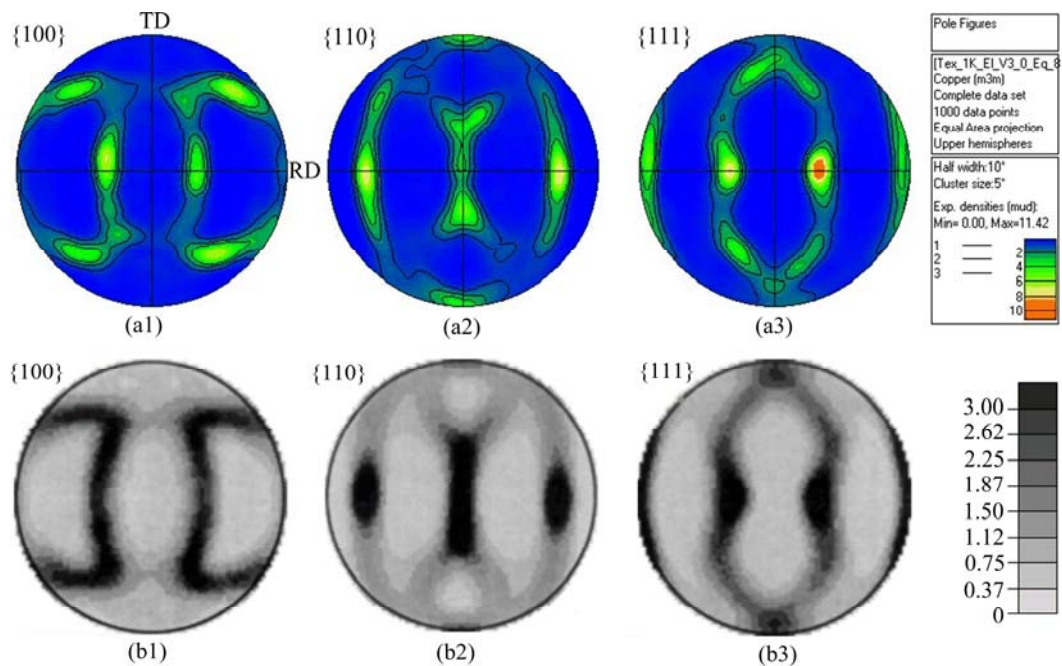


**Fig. 6** Textures in plane-strain compression at true strain of 1.4: (a1–a3) Predictions of planes  $\{100\}$ ,  $\{110\}$  and  $\{111\}$ ; (b1–b3) Experiments of planes  $\{100\}$ ,  $\{110\}$  and  $\{111\}$  [20]

on the  $\{111\}$  plane.

From Sections 3.3 to 3.6, it can be found that the presented model captures all of the important textures in the deformation processes including uniaxial compression, uniaxial tension, simple shear and plane-strain compression. Therefore, the model is reliable to be applied for prediction of texture evolution with varying deformation conditions.

#### 4 Texture evolution with varying deformation conditions

The model was applied to investigate the texture evolution under different conditions. The effects of deformation states, strain rates, and slip systems are studied.

##### 4.1 Effects of deformation states

Different deformation states are achieved by adjusting the ratios of  $V_3$  to  $V_2$ , i.e.  $k=V_3/V_2$ . If there is no constraint on  $V_3$ , the deformation is the uniaxial compression. In this process,  $V_3$  is passive and the texture evolution is illustrated in Fig. 3. When a weak constraint is applied on  $V_3$ , e.g.  $k=-0.43$  ( $V_2$  is negative), the  $\{111\}$  plane texture in Fig. 3 rotates to  $\pm 35^\circ$  to ND along RD, as shown in Fig. 7(a), while the  $\{100\}$  texture maintains the characteristics of that in uniaxial compression. With increasing constraint on  $V_3$  until the plane-strain compression ( $k=0$ ) is achieved, texture

characteristics in uniaxial compression disappear completely (as shown in Fig. 6). When the constraint on  $V_3$  enhances further, e.g.  $k=0.14$ ,  $k=0.43$  and  $k=0.71$  (both  $V_2$  and  $V_3$  are negative), the strong textures progress from  $\pm 35^\circ$  to ND in plane-strain compression to fiber texture along RD direction on the  $\{111\}$  plane, as shown in Figs. 7(b)–(d). It shows varying deformation states change grain orientations and thus textures remarkably. Additionally, the texture intensity shows an increasing tendency with the increase of  $k$ .

##### 4.2 Effects of strain rates

Moreover, the strain rate of deformation does affect on texture evolution. As our study, the texture types and the positions of strong texture do not change with strain rate. However, the intensity of texture reduces with the increase of strain rate, as shown in Fig. 8. It can be found that the texture intensity drops dramatically when the strain rate increases from  $10^{-1} \text{ s}^{-1}$  to  $10^2 \text{ s}^{-1}$ , while the reduction slows down when the strain rate increases from  $10^2 \text{ s}^{-1}$  to  $7 \times 10^4 \text{ s}^{-1}$ . It can be explained that the large strain rate makes no enough time for grain orientation rotation in the first range. Then, in the second range, the strain rate has already reached a high level, i.e., there has not been enough time for grain orientation rotation.

##### 4.3 Effects of slip systems

Generally, only  $12\langle 111 \rangle(110)$  slip systems participate

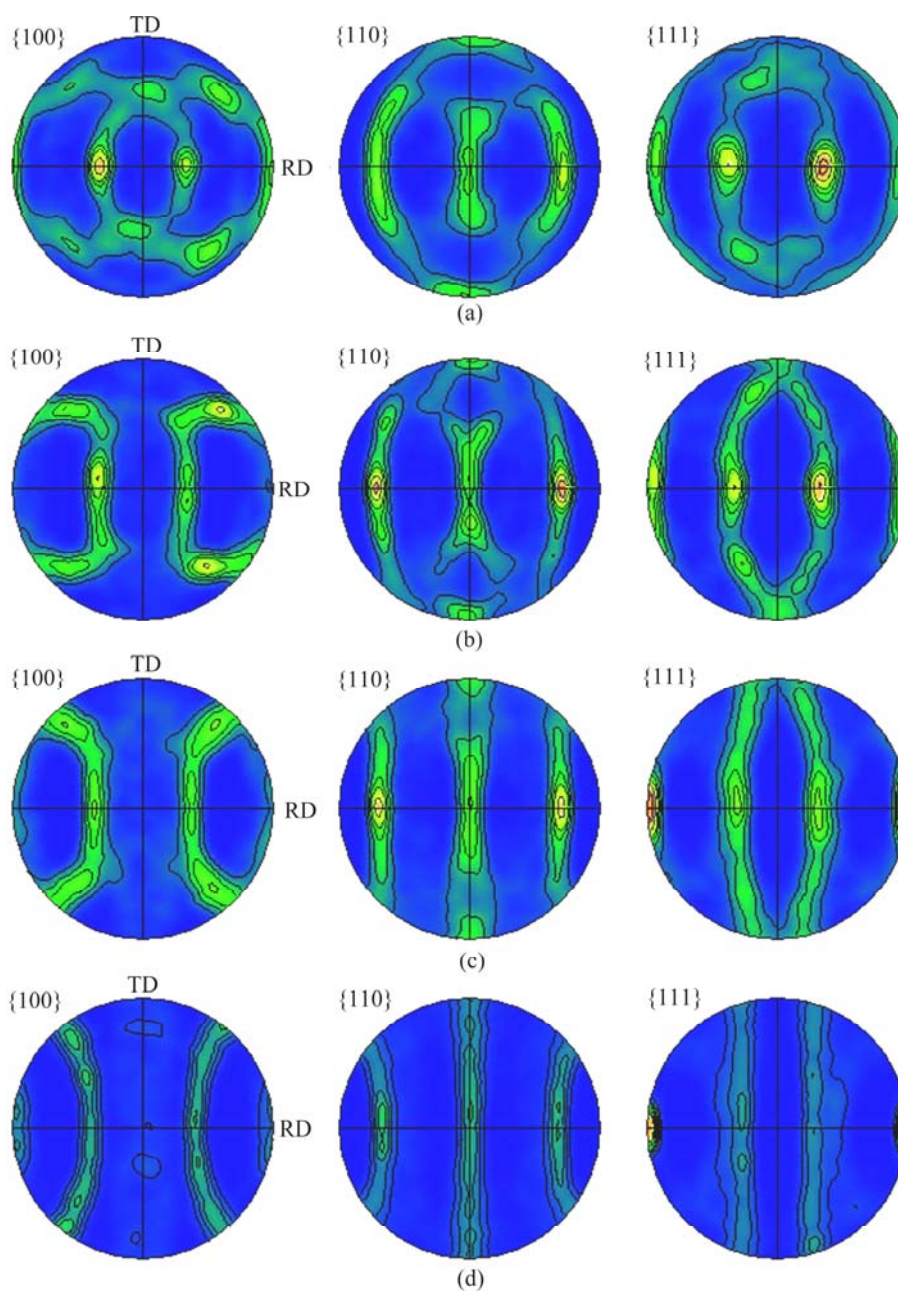


**Fig. 7** Effects of deformation states on textures on planes {100}, {110} and {111}: (a1–a3)  $k=-0.43$ ; (b1–b3)  $k=0.14$ ; (c1–c3)  $k=0.43$ ; (d1–d3)  $k=0.71$

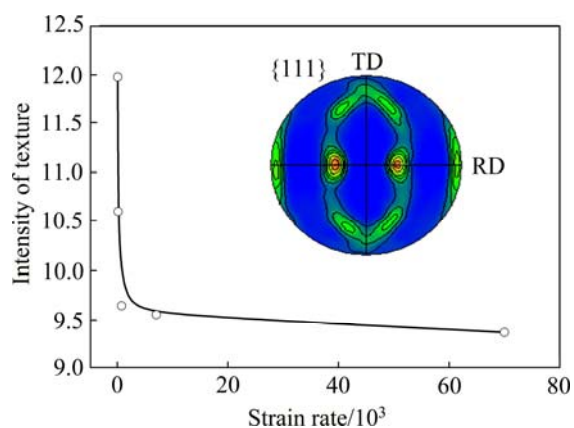


**Fig. 8** Effects of strain rates on textures

the deformation of a face-centered cubic (FCC) metal. However, the experimental observation finds that  $\langle 100 \rangle (011)$  slip systems are activated in deformation of FCC metals. So, here, different slip systems are considered to study their effects on textures. Figure 9 shows much more relaxed textures in terms of orientations distribution and texture intensity in case of  $12 \langle 111 \rangle (110) + 6 \langle 100 \rangle (011)$  slip systems. It is because more slip systems participating deformation improve the deformation anisotropy of a grain; more homogeneous deformation cause less orientations rotating to the referred orientation.

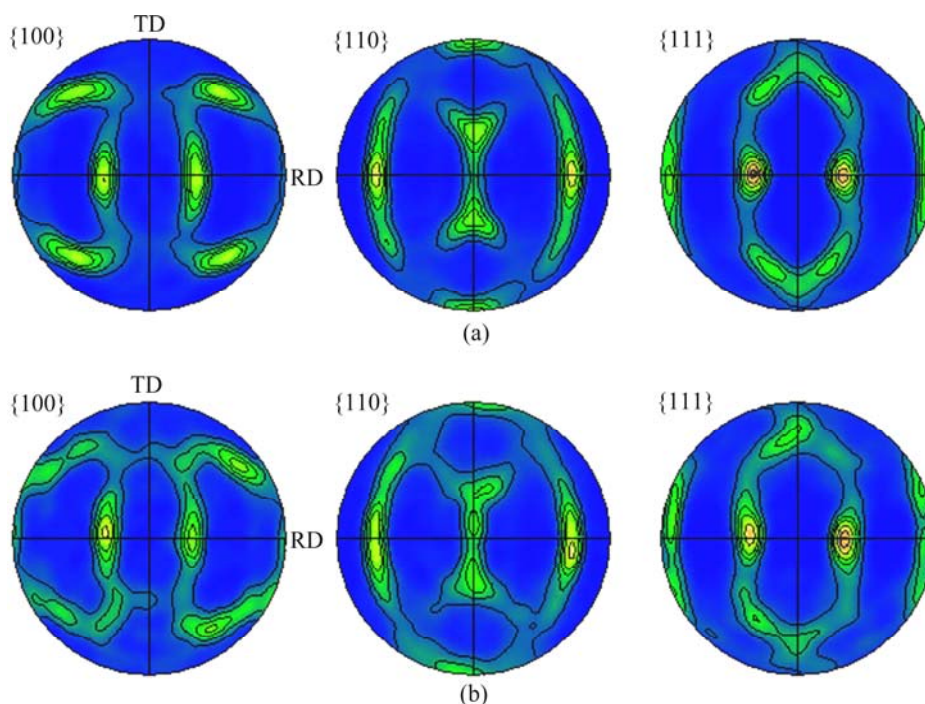


**Fig. 9** Effects of slip systems participating calculation on textures on planes  $\{100\}$ ,  $\{110\}$  and  $\{111\}$ : (a1–a3)  $12\langle 111\rangle(110)$ ; (b1–b3)  $12\langle 111\rangle(110)+6\langle 100\rangle(011)$

## 5 Conclusions

1) An explicit model controlled by a linear equations set was developed. Crystallographic-system based solving procedure was proposed and the complete pivot Gaussian elimination method was adopted for solution. The model was proved much more efficient (more than 100 time) than the implicit model.

2) The model captures all of the important textures by comparing with the experimental results in the deformation processes as uniaxial compression, uniaxial tension, simple shear and plane-strain compression.

3)  $\{111\}$  plane texture progressed to  $\pm 35^\circ$  to ND to  $\{111\}$  fiber texture with increasing  $k$ . High strain rate does not change texture types but makes textures weak.  $12\langle 111\rangle(110)+6\langle 100\rangle(011)$  slip systems participating calculation make the predicted texture more relaxed than only  $12\langle 111\rangle(110)$  slip systems.

## References

- [1] CHEN Jian, YAN Wen, LI Wei, MIAO Jian, FAN Xin-hui. Texture evolution and its simulation of cold drawing copper wires produced by continuous casting [J]. Transactions of Nonferrous Metals Society of China, 2011, 21(1): 152–158.
- [2] ROTERS F, EISENLOHR P, HANTCHERLI L, TJAHAJANTO D D, BIELER T R, RAABE D. Overview of constitutive laws, kinematics, homogenization and multiscale methods in crystal plasticity finite-element modeling: Theory, experiments, applications [J]. Acta Materialia, 2010, 58(4): 1152–1211.
- [3] KALIDINDI S R, BRONKHORST C A, ANAND L. Crystallographic texture evolution in bulk deformation processing of FCC metals [J]. J Mech Phys Solids, 1992, 40(2): 537–569.
- [4] LI H W, YANG H, SUN Z C. A robust integration algorithm for implementing rate dependent crystal plasticity into explicit finite element method [J]. Int J Plasticity, 2008, 24(2): 267–288.
- [5] LÜ L X, ZHEN L. Crystal plasticity simulation of polycrystalline aluminum and the effect of mesh refinement on mechanical responses [J]. Mater Sci Eng A, 2011, 528(22–23): 6673–6679.
- [6] RAPHANEL J L, RAVICHANDRAN G, LEROY Y M. Three-dimensional rate-dependent crystal plasticity based on Runge-Kutta algorithms for update and consistent linearization [J]. International Journal of Solids and Structures, 2004, 41(22–23): 5995–6021.
- [7] PIERCE D, ASARO R J, NEEDLEEMAN A. Material rate dependence and localized deformation in crystalline solids [J]. Acta Metall, 1983, 31(12): 1951–1976.
- [8] GRUJICIC M, BATCHU S. Crystal plasticity analysis of earing in deep-drawn OFHC copper cups [J]. J Mater Sci, 2002, 37(4): 753–764.
- [9] TAYLOR G I. Plastic strain in metals [J]. Journal of the Institute of Metals, 1938, 62: 307–324.
- [10] Van HOUTTE P, DELANNARY L, KALIDINDI S R. Comparison of two grain interaction models for polycrystal plasticity and deformation texture prediction [J]. Int J Plasticity, 2002, 18(3): 359–377.
- [11] Van HOUTTE P, LI S, SEEFELDT M, DELANNAY L. Deformation texture prediction: From the Taylor model to the advanced Lamel model [J]. Int J Plasticity, 2005, 21(3): 589–624.
- [12] MAHESH S. A binary-tree based model for rate-independent polycrystals [J]. Int J Plasticity, 2010, 26(1): 42–64.
- [13] KUMAR M A, MAHESH S, PARAMESWARAN V. A ‘stack’ model of rate-independent polycrystals [J]. Int J Plasticity, 2011, 27(6): 962–981.
- [14] NEIL C J, AGNEW S R. Crystal plasticity-based forming limit prediction for non-cubic metals: Application to Mg alloy AZ31B [J].

- Int J Plasticity, 2009, 25(3): 379–398.
- [15] HUANG Shi-yao, ZHANG Shao-ru, LI Da-yong, PENG Ying-hong. Modeling texture evolution during rolling process of AZ31 magnesium alloy with elasto-plastic self consistent model [J]. Transactions of Nonferrous Metals Society of China, 2011, 21(6): 1348–1354.
- [16] HUANG Shi-yao, ZHANG Shao-ru, LI Da-yong, PENG Ying-hong. Simulation of texture evolution during plastic deformation of FCC, BCC and HCP structured crystals with crystal plasticity based finite element method [J]. Transactions of Nonferrous Metals Society of China, 2011, 21(8): 1817–1825.
- [17] RAABE D, BECKER R C. Coupling of a crystal plasticity finite-element model with a probabilistic cellular automaton for simulating primary static recrystallization in aluminium [J]. Model Simul Mater Sci Eng, 2000, 8(6): 445–462.
- [18] ZHOU Y, NEALE K W, TÓTH L S. A modified model for simulating latent hardening during the plastic deformation of rate-dependent FCC polycrystals [J]. Int J Plasticity, 1993, 9(8): 961–978.
- [19] ABAQUS [M]. Version 6.10. Providence, RI: ABAQUS, Inc., 2010.
- [20] BRONKHORST C A, KALIDINDI S R, ANAND L. Polycrystalline plasticity and the evolution of crystallographic texture in FCC metals [J]. Phil Trans R Soc Lond, 1992, A341(1662): 443–477.

## 基于晶体塑性有限元方法的不同变形状态下织构演化预测

李宏伟, 杨 合

西北工业大学 凝固技术国家重点实验室, 西安 710072

**摘 要:** 提出一种以线性方程组为控制方程的显式晶体塑性模型。该模型可用高斯全主元消去法直接求解, 无需任何迭代。提出基于晶体学坐标系的求解流程以减少由于变形中晶粒旋转而额外增加的计算量。建立晶体塑性有限元模型, 并将预测结果与试验结果进行对比, 验证该模型在织构演化预测方面的可靠性。该模型被用于预测不同变形状态下的织构演化, 而这些不同的变形状态是通过调整  $Z$  和  $Y$  方向上的加载速度比( $k$ )实现的。实验结果表明: 该模型在织构演化预测方面是可靠的(在压缩、拉伸、简单剪切和平面应变压缩过程中的预测结果与试验吻合良好)和高效的(比隐式模型快 100 多倍); 随着  $k$  值的增大, 强织构由与法向(ND)成 $\pm 35^\circ$ 角向 $\{111\}$ 面上的丝织构转变, 且织构强度增大; 当应变速率在  $0.1\sim 100\text{ s}^{-1}$  之间增大时, 织构强度迅速降低, 而当应变速率在  $100\sim 7\times 10^4\text{ s}^{-1}$  之间增大时, 织构强度缓慢减小, 这表明该模型在模拟超高应变速率变形时也是数值稳定的。

**关键词:** 晶体塑性; 织构演化; 变形状态; 应变速率; 显式模型

(Edited by DENG Lü-xiang)